

pubs.acs.org/JACS Article

Role of the Perfluoro Effect in the Selective Photochemical Isomerization of Hexafluorobenzene

Jordan M. Cox,§ Matthew Bain,§ Michael Kellogg, Stephen E. Bradforth,* and Steven A. Lopez*



Cite This: J. Am. Chem. Soc. 2021, 143, 7002-7012



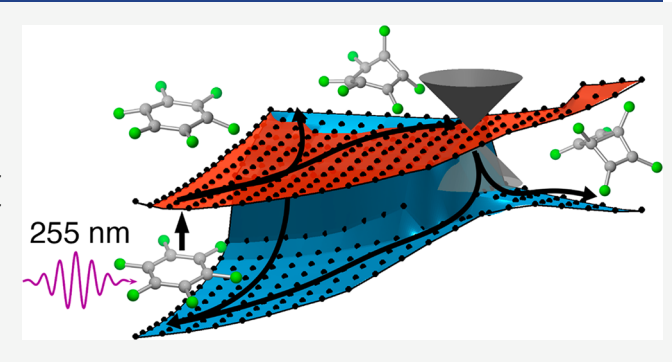
ACCESS

Metrics & More



3 Supporting Information

ABSTRACT: Hexafluorobenzene and many of its derivatives exhibit a chemoselective photochemical isomerization, resulting in highly strained, Dewar-type bicyclohexenes. While the changes in absorption and emission associated with benzene hexafluorination have been attributed to the so-called "perfluoro effect", the resulting electronic structure and photochemical reactivity of hexafluorobenzene is still unclear. We now use a combination of ultrafast time-resolved spectroscopy, multiconfigurational computations, and non-adiabatic dynamics simulations to develop a holistic description of the absorption, emission, and photochemical dynamics of the 4π -electrocyclic ring-closing of hexafluorobenzene and the fluorination effect along the reaction coordinate. Our



calculations suggest that the electron-withdrawing fluorine substituents induce a vibronic coupling between the lowest-energy $^1B_{2u}$ ($\pi\pi^*$) and $^1E_{1g}$ ($\pi\sigma^*$) excited states by selectively stabilizing the σ -type states. The vibronic coupling occurs along vibrational modes of e_{2u} symmetry which distorts the excited-state minimum geometry resulting in the experimentally broad, featureless absorption bands, and a \sim 100 nm Stokes shift in fluorescence—in stark contrast to benzene. Finally, the vibronic coupling is shown to simultaneously destabilize the reaction pathway toward hexafluoro-benzvalene and promote molecular vibrations along the 4π ring-closing pathway, resulting in the chemoselectivity for hexafluoro-Dewar-benzene.

■ INTRODUCTION

The synthesis of polyacetylene sparked the field of organic electronics, despite difficulties in processing polyacetylene and its high propensity to be oxidized when exposed to air. 1,2 As early as 1979, polymer chemists have sought to circumvent these challenges, especially its instability, with a strategy of fluorination. Theoretical calculations predict that the electronwithdrawing fluorines significantly reduce the oxidation rate by lowering the frontier molecular orbitals of polyacetylene and minimizing overlap with those of molecular oxygen. However, synthesizing fluorinated polyacetylenes has proven difficult by the traditional means of polymerizing fluorinated acetylene. Not only is difluoroacetylene an explosive and pyrophoric gas, but polymerization results in a highly irregular material that contains a mixture of -CF, -CF₂, and -CF₃ functional groups. Burns and co-workers⁴ recently achieved this elusive synthesis by leveraging the mechanochemical "unzipping" of highly strained ladderene polymers to form partially fluorinated polyacetylenes. The key step in their synthetic scheme is the formation of a fluorinated ladderene, achieved through a photochemical cascade reaction, involving a hexafluorobenzene (HFB) [2 + 2]-cycloaddition, followed by a disrotatory 4π electrocyclic ring-closing of the hexafluorinated diene intermediate (Figure 1b). This fluorinated ladderene is then polymerized and mechanochemically unzipped to yield fluorinated polyacetylene (Figure 1c).

The 4π electrocyclic ring-closing reaction is known for many highly fluorinated cyclic polyenes, many of which result from cycloadditions with HFB.⁶⁻⁹ HFB itself undergoes the same ring-closing reaction, 10 photochemically isomerizing to hexafluoro-Dewar-benzene (Dewar-HFB) chemoselectively. The hexafluoro-benzvalene or -fulvene isomers are not observed, but are the major products of benzene photochemistry (Figure 1a). 11,12 HFB also shows significantly different photophysical behavior than benzene; its absorption spectrum has a broad, featureless absorption band and a substantial (100 nm) Stokes shift in the emission band, even in the gas phase. 13 These dramatic changes in photophysics have been attributed to the "perfluoro effect". 14 The stark contrast in the photochemical outcomes of HFB and benzene photochemistries suggests that the perfluoro effect also plays an important role as HFB isomerizes to Dewar HFB.

The chemoselective isomerization of HFB was first reported in 1966 when Haller and Camaggi^{10,15} independently reported

Received: February 7, 2021 Published: May 3, 2021





Figure 1. (A) Photochemical isomerization reactions of benzene and HFB yielding different product distributions.⁵ (B) Photochemical cascade reaction of Burns and co-workers to form a fluorinated ladderene.⁴ (C) Subsequent polymerization and mechanochemical unzipping of the fluorinated ladderene to form fluorinated polyacetylene.

the reaction. Further work by Haller determined that the quantum yield of the gas-phase isomerization was \leq 3%, under pressures ranging from 44 to 1052 Torr. The quantum yield was unchanged in the presence of a triplet sensitizer, O_2 . This suggests that the reaction proceeds entirely in the singlet manifold. Picosecond transient absorption (TA) spectroscopy indicates the possibility of diradical or charge-transfer intermediates, though the role of these species in the photochemistry is still unknown. This quantum yield is low compared to other examples of 4π electrocyclic ring-closing reactions where quantum yields can reach 17%.

Laser-induced fluorescence measurements by Zgierski et al. show that benzene perfluorination substantially lowers the energies of the C–F σ and σ^* orbitals. In fact, Zgierski proposes that in HFB, the σ -type orbital stabilization is sufficient to reverse the $\pi\pi^*$ and $\pi\sigma^*$ state-ordering relative to benzene and that the S_1 state in HFB is of $\pi\sigma^*$ character. The $\pi\sigma^*$ S_1 assignment has been used by Zgierski and Temps S_1 to explain the large Stokes shift by assigning the gap between the absorption and emission onsets to an optically dark $S_0 \rightarrow S_1$ transition of $\pi\sigma^*$ character. This idea has been used to explain the low fluorescence yield and short fluorescence lifetime of HFB. Philis et al., Motch et al., and Holland et al. instead agree that the S_1 and S_2 states are $\pi\pi^*$ and $\pi\sigma^*$, respectively, based on photoabsorption and photoelectron spectroscopy measurements.

Mondal et al. pioneered theoretical work on HFB dynamics, describing the initial ultrafast $S_N \rightarrow S_1$ relaxation processes, and used equation-of-motion coupled-cluster (EOM-CCSD) calculations to support the S_1 assignment of Philis, Motch, and Holland. However, a model of the photophysics and photochemistry of HFB which unifies the current reported observations does not yet exist. Developing this unified description would lay the foundation for design rules of highly strained compounds that leverage the chemoselective photoisomerization of HFB and its derivatives. This work utilizes ultrafast time-resolved spectroscopic studies, multireference calculations, and nonadiabatic molecular dynamics simulations

to clarify the photophysics and origin of the low yielding, chemoselective isomerization to Dewar-HFB. While this photochemical reaction is synthetically useful,⁴ this work shows why this photochemical reaction is inefficient and emphasizes the difficulty in tracking such reaction pathways.

■ RESULTS AND DISCUSSION

The density of frontier excited states and the highly symmetric D_{6h} structure of HFB has generated substantial debate in the literature about the nature of the light-induced electronic transitions. The $\pi\pi^*$ or $\pi\sigma^*$ character of these states dictates the shape of the potential energy surface which directs the photochemistry. Without a full understanding of the order and interplay between the molecular excited states of HFB, a clear understanding of the inefficient yet chemoselective reactivity has remained elusive.

Figure 2 shows the overlay of the experimental absorption spectrum for HFB solvated in ethanol and the simulated gasphase absorption spectrum, with the contributions of each of the four lowest-energy electronic states to the simulated spectrum. The steady-state solution-phase UV—vis absorption spectrum, shown by the dashed gray trace, was measured for a 75 μ M solution of HFB in ethanol. The molar absorptivities in the measured transitions lie in the 200–600 M⁻¹ cm⁻¹ range, indicating that HFB is a relatively weak absorber for these lowest energy transitions—an intuitively undesirable quality in a photochemical reagent.

The simulated gas-phase absorption spectrum, the solid black trace, was computed at the extended multistate XMS-CASPT2(6,7)/aug-cc-pVDZ level of theory based on 164 HFB geometries randomly sampled from a 1 ps SA-10-CAS(6,7)/6-31G molecular dynamics trajectory propagated in the ground state at 300 K in vacuum. As the ground state equilibrium HFB structure has no net dipole moment, precluding solvent dipole interactions, no polarizable continuum models were included in the calculation. More sophisticated explicit solvent models were deemed too computationally expensive at this time. The absorption line-spectrum computed at the XMS-CASPT2-

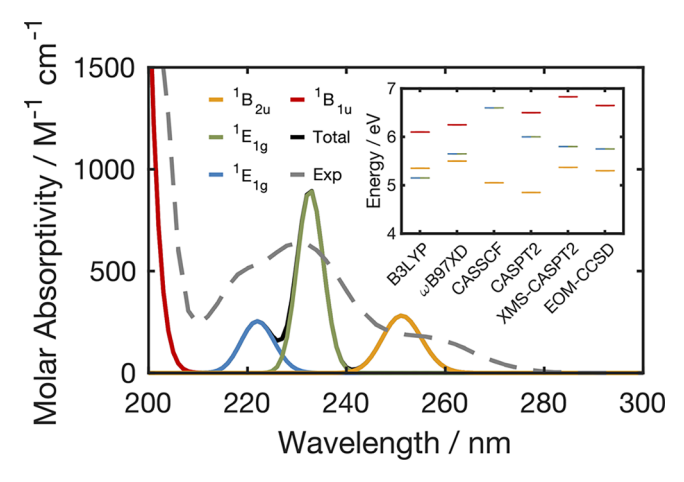


Figure 2. Theoretically computed gas-phase absorption of HFB in black and the measured UV—vis absorption spectrum of HFB solvated in ethanol in dashed gray. The transition-specific computed spectra are rendered below in solid-colored lines with upper state symmetry assignments shown in the legend. The inset panel shows the vertical excitation energies for the four lowest excited states of HFB. All calculations used the aug-cc-pVDZ basis set, CAS and (XMS-CASPT2) calculations included a (6, 7) active space described in the Experimental Section.

 $(6,7)/{\rm aug\text{-}cc\text{-}pVDZ}$ level for the $D_{6h}\text{-}{\rm symmetric}$ minimum geometry predicts absorption oscillator strengths of 1.7×10^{-5} and 7.6×10^{-5} for the $^{1}{\rm B}_{2\rm u}$ and $^{1}{\rm B}_{1\rm u}$ $(\pi\pi^*)$ states, respectively, and 1.9×10^{-9} for the $^{1}{\rm E}_{1\rm g}$ $(\pi\sigma^*)$ state. The computed absorption spectrum in Figure 2 encompasses geometries that break the D_{6h} symmetry leading to substantially higher average oscillator strengths of 6.7×10^{-3} and 2.4×10^{-3} for the two $^{1}{\rm E}_{1\rm g}$ states, which is comparable to the $^{1}{\rm B}_{2\rm u}$ and $^{1}{\rm B}_{1\rm u}$ states at 3.2×10^{-3} and 9.0×10^{-2} , respectively.

Absorption Spectrum. The colored curves in Figure 2 show the contributions to the total gas-phase absorption spectrum computed for each of the four lowest-energy electronically excited states. The calculated absorption spectrum suggests that the lowest-energy excited state is the $^{1}\mathrm{B}_{2\mathrm{n}}$ $(\pi\pi^{*})$ state and that the absorption peaks at 230 and 220 nm arise from splitting of the ${}^{1}E_{1g}$ ($\pi\sigma^{*}$) state. This assignment matches the previous experimental work of Philis, Motch, and Holland and the theoretical work of Mondal. Mondal demonstrated that the splitting of the ${}^{1}E_{1g}$ state resulted from the Jahn-Teller effect but disagrees with Temps and coworkers who assign the ${}^{1}E_{1g}$ state as S_{1} . The Temps assignment is bolstered by providing an intuitive explanation of the large gap between the absorption and emission onsets of 100 nm by suggesting that this gap arises instead from emission from a low-lying ${}^{1}E_{1g}$ ($\pi\sigma^{*}$) dark state centered at around 280 nm. Therefore, for the assignment of S_1 as $\pi\pi^*$ to be correct, an unusually large Stokes shift would require an S₁ potential energy surface where the excited state minimum geometry is significantly different from the ground state minimum—a potentially important observation in understanding the photo-

To determine the origins of the 100 nm Stokes shift observed in the absorption/fluorescence spectra of HFB, we present the absorption and fluorescence emission spectra of a 75 μ M solution of HFB in ethanol with a solid red line (absorption) and red filled trace (fluorescence) in the main panel of Figure 3.

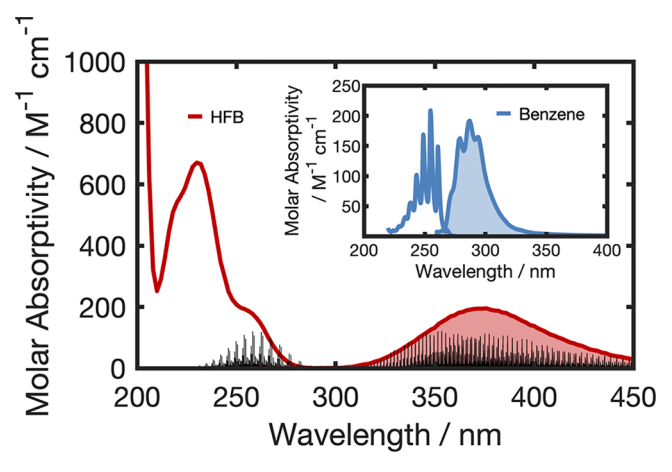


Figure 3. Absorption and emission spectra for hexafluorobenzene (red, main panel) and benzene (blue, inset panel). Absorption spectra are rendered in solid lines and emission spectra in filled traces. Both absorption and emission spectra for hexafluorobenzene are measured using a 75 μ M solution in ethanol, while the analogous benzene spectra are adapted from Du et al.²⁴ and the extinction values calibrated by Berlman.²⁵ The black stick spectra represent vibrationally resolved absorption and emission spectra computed from Franck—Condon factors of the ground- and $^{1}B_{2u}$ excited state gasphase minimum structures. Franck—Condon factors are computed using the parallel mode approximation at 0 K.

Vibrationally Resolved Electronic Spectra. Beneath these experimental traces is a black stick spectrum showing the computed vibrationally resolved absorption and emission spectra between the ${}^{1}A_{1g}$ and ${}^{1}B_{2u}$ ($\pi\pi^{*}$) states of the isolated molecule. The inset panel shows the equivalent spectra for benzene in blue, where the absorption and fluorescence were adapted from Du et al.²⁴ and the absorption scaled by the Berlman extinction coefficient.²⁵ The vibrationally resolved electronic spectra were simulated by computing the Franck-Condon factors for the overlap between the ${}^{1}A_{1g}$ and ${}^{1}B_{2u}$ state vibrational wavefunctions using the harmonic approximation as implemented in ezSpectrum. 26 These computed spectra consider the 13 modes with most significant Franck-Condon activity (vide infra) and includes up to 21 and 30 vibrational quanta in these modes for the absorption and emission spectra, respectively. Figure 3 shows the overlay of the experimental and simulated vibrationally resolved electronic spectra. The full set of vibrational modes and their corresponding frequencies are shown in Table S1 of the Supporting Information (SI). The Franck-Condon overlap between the ¹A_{1g} and ¹B_{2u} states suffices to explain the origin of the large Stokes shift of 1.3 eV (260-360 nm) between the absorption and emission spectra. This computed value slightly underestimates the experimentally measured Stokes shift of 1.56 eV. This conclusively demonstrates that the Stokes shift is an inherent feature of the ¹B_{2u} state, rather than an artifact from a dark emissive state.

The large value of the Stokes shift is equivalent to recognizing there is a large displacement along one or more vibrational modes. Our analysis of the vibrationally resolved electronic spectra, shows the most intense absorption and emission features deposit 10 and 14 vibrational quanta in the excited-state and ground-state, respectively. These vibrational quanta are distributed through several combination progressions and predominantly activate the ν_{18} and ν_{19} modes, as rendered in Table S1 and using the Herzberg notation. These modes have e_{2u} symmetry in D_{6h} and correspond to out-

of-plane bending of the para-oriented carbon and fluorine atoms, respectively. The selective population of the e_{2u} vibrational modes suggests a symmetry-dependent coupling dominates the absorption and emission spectra.

Electronic State Coupling. We examined the electronic structures and gas-phase minimum energy geometries of the ground and $^{1}B_{2u}$ states and the motions connecting them to understand the origin of the Stokes shift and vibrationally resolved electronic spectra. The left-hand side of Figure 4

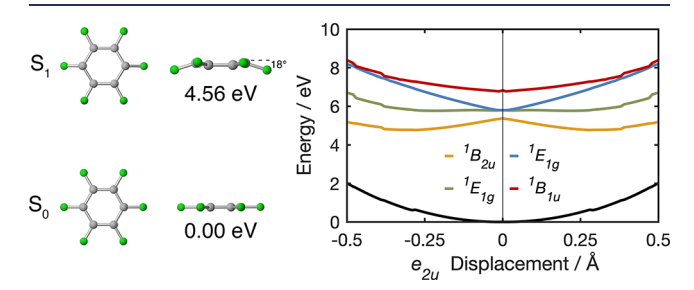


Figure 4. (Left) Side and top elevations of the minimum energy geometries for the S_0 ($^1A_{1g}$) and S_1 ($^1B_{2u}$) states. (Right) Cuts through the ground, $^1A_{1g}$ (black), and first four excited, $^1B_{2u}$ (orange), $^1E_{1g}$ (green), $^1E_{1g}$ (blue), and $^1B_{1u}$ (red), potential energy surfaces, along the ν_{18} e $_{2u}$ motion corresponding to opposing carbons moving symmetrically out of plane.

shows the completely planar D_{6h} geometry of the ground state minimum and the minimum-energy geometry of the $^{1}B_{2u}$ state. The excited state minimum is significantly distorted compared to the high-symmetry ground state geometry. Two of the carbon atoms, with a 1,4 relationship, are visibly distorted out-of-plane, and the fluorine atoms attached to the 1,4-carbons are bent out-of-plane by 18°. This results in a $C_{2\nu}$ symmetric geometry. This is in contrast to calculations of the optimized excited state minima of benzene, where the $^{1}B_{2u}$ minimum-energy geometry is D_{6h} symmetric. This significant geometric distortion from S_0 to S_1 results in the observed Stokes shift by reducing the S_1/S_0 gap by 1.53 eV.

The minimum energy path (MEP) from the Franck–Condon point on the $^1\mathrm{B}_{2\mathrm{u}}$ surface is computed to investigate the evolution of the electronic structure of HFB along this geometric distortion. There is a sudden shift in the multiconfigurational nature of the CAS wavefunction along the MEP upon breaking the D_{6h} symmetry (see Figure S1). The wavefunction is entirely comprised of $\pi\pi^*$ configurations while the molecule is D_{6h} symmetric; symmetry breaking along the MEP induces $\pi\sigma^*$ mixing. The maximum $\pi\sigma^*$ contribution to the total wavefunction is 6.6%. Taken together, the $\pi\pi^*$ and $\pi\sigma^*$ configuration mixing with the symmetry-breaking distortion suggest that the $^1\mathrm{B}_{2\mathrm{u}}$ state is vibronically coupled with the energetically nearby $^1\mathrm{E}_{1\mathrm{g}}$ $(\pi\sigma^*)$ state.

As this coupling should occur via e_{2u} vibrational modes, an energy plot of the ground-state and the first four excited-states with respect to e_{2u} normal mode displacement is shown in the right of Figure 4. The orange trace shows the double-well stabilization of the ${}^{1}B_{2u}$ state when displaced along the e_{2u} symmetric modes leading to the distorted minimum energy geometry. The blue and green traces represent the splitting of the two components of the ${}^{1}E_{1g}$ state. Given this observation, one would have expected the harmonic approximation used above to perform poorly for the excited state double well potential, so the good agreement between the computed vibronic absorption band and the first experimental absorption

band rendered in Figure 3 is somewhat surprising. Previous work has shown that the vibronic coupling constant between the $^{1}\mathrm{B}_{2\mathrm{u}}$ and $^{1}\mathrm{E}_{1\mathrm{g}}$ states is 0.1548 and 0.0619 eV for coupling through modes ν_{18} and ν_{19} , respectively. 23 The cross-section of the potential energy surface (PES) in Figure 4 shows that the combination of the vibronic coupling constant and the low energy gap is sufficient to induce the instability of the D_{6h} geometry of the HFB $^{1}\mathrm{B}_{2\mathrm{u}}$ state with respect to distortions along the $\mathrm{e}_{2\mathrm{u}}$ modes. We conclude that the small energy gap (0.42 eV) between the $^{1}\mathrm{B}_{2\mathrm{u}}$ and $^{1}\mathrm{E}_{1\mathrm{g}}$ states in the FC region results from the perfluoro effect, implying that the Stokes shift, results from the perfluoro effect via a pseudo-Jahn–Teller distortion in the $^{1}\mathrm{B}_{2\mathrm{u}}$ minimum geometry leads to Dewar-HFB, implying that this coupling encourages Dewar-HFB formation.

Transient Absorption Spectroscopy. With the multiconfigurational calculations reproducing the experimental photophysical processes in HFB, the photochemical isomerization of HFB to Dewar-HFB is now considered. Figure 5

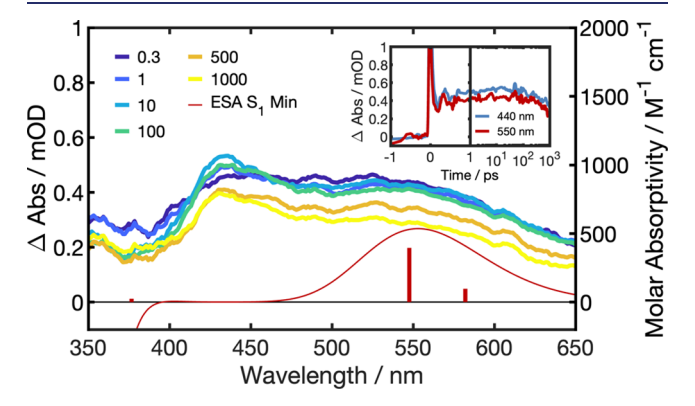


Figure 5. Transient absorption spectra for 200 mM HFB in ethanol. The main panel shows transient absorption spectra at pump—probe delays indicated by the color-coded legend (in picoseconds) following photoexcitation at 255 nm (4.86 eV). The inset shows the time evolution on a linear scale from -1 to 1 ps pump—probe delay and a logarithmic scale from 1 to 1000 ps delays. For sticks and simulated bands see the text.

shows the experimental transient absorption spectrum of a 200 mM solution of HFB in ethanol recorded following excitation with a 255 nm UV laser pulse (580 nJ). This wavelength was selected to match the 255 nm lamps employed in gram scale reactors for these syntheses. The transient absorption spectrum is rendered at a series of pump—probe delays denoted by the color-coordinated legend. The stick spectrum represents the computed gas-phase excited state absorption spectrum at the S₁ minimum energy geometry. Each absorption peak in the stick spectrum was convoluted with a Gaussian function with an (arbitrary) full-width half-max of 0.2 eV, which yielded the simulated absorption spectrum shown by the red trace. The corresponding contour plot and the full range of pump—probe delays are rendered in Figure S2 and Table S2.

By analyzing the ground state absorption spectrum (Figure 2), approximately 3% of the molecules excited at 255 nm are estimated to be promoted to the S_2 $^1E_{1g}$ state and 97% promoted to the S_1 $^1B_{2u}$ state. The transient spectrum contains two excited-state absorption features longer than 400 nm, overlapping a (negative) stimulated emission band peaking at 375 nm (compare to fluorescence band in Figure 3). The

excited-state absorption from S_1 features a broad absorption peak centered at 550 nm that immediately rises and a sharper, more intense absorption centered at 440 nm, which rises to 90% of its maximum intensity instantaneously and then subsequently rises to 100% over \sim 10 ps.

A broad 550 nm absorption has previously been assigned to a biradical form of HFB based upon then-current CNDO/S calculations.¹⁷ We prefer the assignment to an excited state S₁ because stimulated emission is simultaneously observed. Our new multiconfigurational calculations predict an excited-state spectrum based on the S₁ minimum geometry. This spectrum shows two dominant absorption peaks at 540 and 590 nm. These peaks correspond, in C_{2V} symmetry, to the $S_1(^1B_1) \rightarrow S_3$ $(^{1}B_{1})$ and S_{1} $(^{1}B_{1}) \rightarrow S_{4}$ $(^{1}A_{1})$ transitions, respectively. These two transitions from the S₁ minimum overlap to form one peak and better explain the broad absorption feature at 550 nm in the experimental spectrum. On the basis of the conditions in our experiment, we calculate ~0.04% of HFB molecules are photoexcited. The XMS-CASPT2/aug-cc-pVDZ calculations predict oscillator strengths of 0.0014 and 0.0057 for the $S_1(^1B_1) \rightarrow S_3(^1B_1)$ and $S_1(^1B_1) \rightarrow S_4(^1A_1)$, respectively. From these values, and the estimated concentration of excitedstate molecules, an excited state molar absorptivity of 500, and in turn, an excited state optical density of 0.5 mOD are predicted. Both values agree well with the recorded transient absorption measurement. This calculation can be reproduced from eqs S1 and S2. However, an assignment for the 440 nm peak is more difficult because it is absent from the computed

Turning to the 440 nm spectral feature, a rising absorption could be assigned to a new absorbing species formed by a bimolecular process. (Figure S3 shows that the sharpening of the 440 nm feature cannot be explained simply as a weakening subtractive effect from the nearby stimulated emission peak narrowing following the cooling of the solvent environment.) A rising band centered at this same wavelength has previously been assigned by Varma et al. to both cation and anion absorption bands using CNDO/S calculations. 17 Varma thus speculated that charge transfer occurs between HFB pairs during the 10 ps rise-time, consistent with the diffusion time scale of charge transfer partners finding one another. EOM-IP-CCSD/aug-cc-pVDZ and EOM-EA-CCSD/aug-cc-pVDZ calculations of the isolated cation and anion absorption bands, respectively, predict that within the 350-650 nm spectral range of the TA experiment, the cation has a single strong absorption centered at 385 nm (3.23 eV) with an oscillator strength of 0.13. In contrast, the anion has three strong absorption bands at 483 nm (2.57 eV), 445 nm (2.78 eV), and 368 nm (3.37 eV) with oscillator strengths of 0.19, 0.14 and 0.077, respectively. The computed bands and their oscillator strengths are summarized in Table S3. These oscillator strengths are $\sim 10^4$ stronger than the excited state absorption bands. If correct, they must belie a correspondingly lower concentration of charge transfer contact pairs to yield optical densities on the same order as the S₁ excited state absorption. The anion band predicted at 445 nm provides an explanation for the 440 nm band in the TA spectrum. However, the conspicuous lack of a corresponding cation peak at 386 nmwhich would also need to show the same 10 ps rise timebrings this assignment into question. Moreover, transient absorption data recorded in nonpolar cyclohexane, shown in Figures S4 and S5, shows no diminishment or shifting of the

440 nm band, as one would expect when a polar environment does not stabilize charged species.

Eximer formation may explain the time-delayed 440 nm absorption band.²⁹ Such rearrangement from a ground-state T-shape to an excited-state slip-stacked arrangement of two aromatic rings occurs on a 10⁻¹⁸ ps time scale in preformed dispersion-bound dimers of benzene in the gas phase.³⁰ However, in dilute solutions, like those studied here, the dimer formation time scale should increase because of the additional diffusion time required for ring association. The formation time should also scale with HFB concentration; the cyclohexane data in Figures S4 and S5 rises on a comparable time scale despite HFB being 4 times more dilute (Figure S9). The assignment of this peak, therefore, remains somewhat elusive.

The inset panel in Figure 5 shows the spectral intensity at two wavelengths, 440 nm (blue) and 550 nm (red), as a function of pump—probe time delay. The time axis is split with the -1 to 1 ps region rendered linearly, while the 1 to 1000 ps region is plotted logarithmically in time. The majority of the excited-state signal is formed within the experimental instrument response function (IRF) and persists for a lifetime significantly greater than the window of the experiment (1 ns). Although the intensities of the features fall over this time scale, the general spectral shape does not change indicating that all the dynamics observed within the TA window occur on the same singlet state.

We noticed that rapidly damped oscillations appear at both probe wavelengths; these oscillations in the ESA intensity over the first picosecond are fit to a convolution of a damped sine wave and an exponential decay. A rendering of this fit and the resultant constants can be found in Figure S6 and Table S4, respectively, along with the model's fully functional form. The oscillation frequency is $\sim\!110~{\rm cm}^{-1}$, which most closely matches the lowest frequency normal mode ν_{19} (computed as 157 cm $^{-1}$ in the ground state)—one of the two vibrational modes implicated in the vibrationally resolved absorption to the $^{1}\mathrm{B}_{2u}$ state. 93 cm $^{-1}$ oscillations with a longer damping time ($\sim\!1$ ps compared to $\sim\!360$ fs seen here) were also observed in the ion-detected pump—probe experiments of Temps for gasphase HFB and assigned to the same motion. 19

There is no signal in the TA spectra that can be assigned to the Dewar-HFB photoproduct. We would expect Dewar-HFB product to absorb wavelengths much shorter than 350 nm, the edge of the experimental probe window. The maximum transient absorption signal of 0.5 mOD is weak relative to typical molecules measured with this technique. We ascribe this to the weak excited state absorption strengths (1000 $\rm M^{-1}$ cm $^{-1}$), possibly compounded with the low excited state population.

To cross check that a significant fraction of excited state population has not branched at earlier delays than captured in the current ${\sim}50$ fs resolution study, we compared it to the excited state evolution of benzene. The excited state of benzene has no ultrafast deactivation pathways and the quantum yield of the photoproduct channel is ${<}1\%.^{31}$ Thus, picosecond-scale excited state signals in benzene should be attributable to the full excited state population. Using the same computational method as applied to HFB, the calculated excited-state molar absorptivity of benzene is 200 ${\rm M}^{-1}~{\rm cm}^{-1}.$ This is comparable with HFB at 500 ${\rm M}^{-1}~{\rm cm}^{-1}$ allowing estimation of the HFB excited state population if the data is recorded under identical conditions. A comparison of the TA

spectra of benzene (green) and HFB (blue) recorded back-toback in a single experimental run is shown in Figure 6. Both of

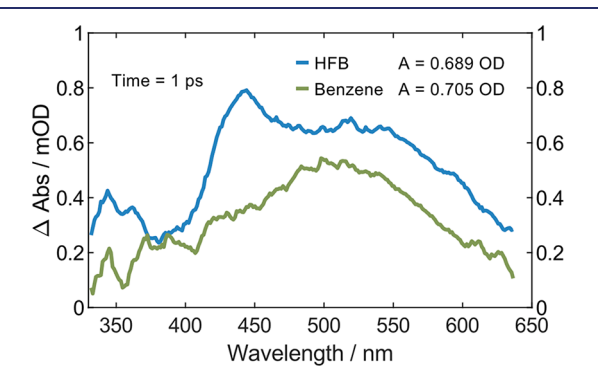


Figure 6. Transient absorption spectra of benzene (green) and HFB (blue) taken 1 ps after excitation with 266 nm. The concentrations of benzene and HFB were \sim 4 M and 400 mM, respectively. These spectra were measured at 1 ps to avoid the rise time of the benzene excimer and intermolecular dynamics.

the transient spectra shown were recorded at a pump—probe delay time of 1 ps to avoid interference either by solvent two-photon absorption at early times or benzene excimer formation at later times. The HFB and benzene solutions were prepared with identical ground state optical densities to ensure the same number of excited state molecules were formed. We measured very similar transient absorbances. This indicates that, similar to benzene, the TA signal captures the majority of the HFB molecules excited, and rules out the possibility of a significant bifurcated flux back to the ground state, or to Dewar-HFB formation, at early times.

Potential Energy Surface. To rationalize the long excitedstate lifetime, the low quantum yield, and chemoselectivity of the HFB 4π -electrocyclic isomerization, we computed the potential energy surface along two independent degrees of freedom toward Dewar-HFB (Figure 7). The reaction coordinates are the out-of-plane angles of two carbon atoms that form the new carbon—carbon σ bond in Dewar-HFB. All other degrees of freedom are allowed to relax for each point on the PES, and the constrained geometries were optimized with SA-10-CASSCF(6,7)/aug-cc-pVDZ. The resulting PESs of the ground and $^{1}B_{2u}$ excited states is shown in Figure 7, along with the geometries of several critical points in the reaction pathway.

The PES shows that both the S_0 and S_1 surfaces feature a broad, energetic minimum centered at 0° and 8° , respectively, though the S_1 surface is significantly flatter. The wide range of available motion in this flat region around the S_1 minimum likely accounts for the fast 360 fs dampening of the oscillations in the transient absorption data. The surfaces also show that there is an S_1/S_0 crossing seam, which lies ≥ 1.4 eV above the S_1 minimum geometry (structure C). This seam corresponds to one out-of-plane angle of $>65^\circ$, and the S_1/S_0 degeneracy persists for geometries where the opposing out-of-plane angle is $<40^\circ$. The geometry of the minimum-energy crossing point (MECP) on this crossing seam is shown as structure D. The two out-of-plane angles in the MECP geometry are 76° and 0° , analogous to the S_1/S_0 MECP in benzene.

Nonadiabatic relaxation from the S_1 state requires at least 1.4 eV more energy than the S_1 minimum, suggesting that this process would proceed slowly—if at all. This is in line with the TA measurements that indicate a long excited-state lifetime. Time Correlated Single Photon Counting (TCSPC) measurements, shown in Figure S7 and Table S5, confirm this lifetime approaches 2.29 ns. The ground-state surface near the crossing seam also shows that relaxation via geometries near the MECP results in a steep path back to the HFB reactant rather than Dewar-HFB. Thus, the crossing seam's productive region lies at higher energies, where the crossing geometry more closely

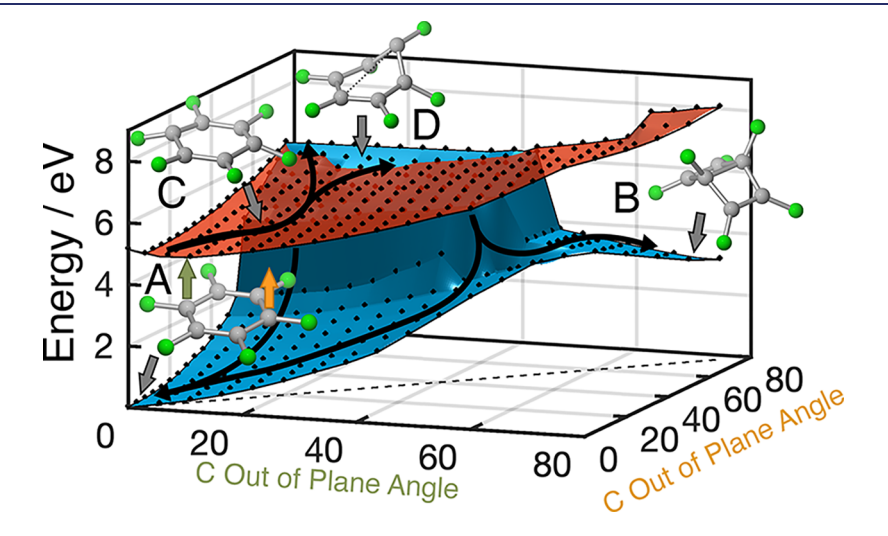


Figure 7. A 2D cut through the $S_0^{-1}A_{1g}$ (blue) and $S_1^{-1}B_{2u}$ (red) gas-phase potential energy surfaces. The two coordinates correspond to the angle of the two para carbons, indicated by the orange and green arrows, rising out of the plane defined by the other four carbons. Motion diagonally across the PES from the D_{6h} minimum in the left-hand corner (A) to the right-hand corner corresponds to both carbons rising symmetrically out of the plane to form the bridgehead bond and yield the Dewar-HFB isomer (B). Here both carbons are out of plane by 76°. Partial motion along the diagonal, where carbons are out-of-plane by 8° and corresponds to the minimum energy geometry of the $^{1}B_{2u}$ state (C). Motion along only one axis, where only one carbon rises out of plane, leads to the MECI at 65° (D). From this MECI, internal conversion to the ground state leads exclusively to the D_{6h} minimum (A). However, from the MECI motion of the other carbon is not degeneracy breaking until 40°. Molecules which pass through the CI at the upper portion of the seam are on a portion of the ground state surface which bifurcates. One trajectory leading back to (A) while the other trajectory leads to the Dewar form (B).

resembles the photoproduct. This region of the seam is up to 0.3 eV higher than the MECP, indicating this process is less favorable than relaxation back to the reactant explaining the low quantum yield for the photoisomerization. It is not however immediately evident from the potential energy surface why hexafluoro-benzvalene is not an observed HFB photoproduct after passing through the MECP in HFB as it is in the analogous benzene.

The branching spaces which define the MECPs in HFB and benzene are analyzed using the first-order approximation of Galván et al. The reaction pathway to benzvalene from the MECP lies along a vector in the branching space, labeled $\hat{\mathbf{g}}$. The relative slope of the PES along $+\hat{\mathbf{g}}$ and $-\hat{\mathbf{g}}$ is shown in Figure 8, along with the MECP geometry and atom-wise

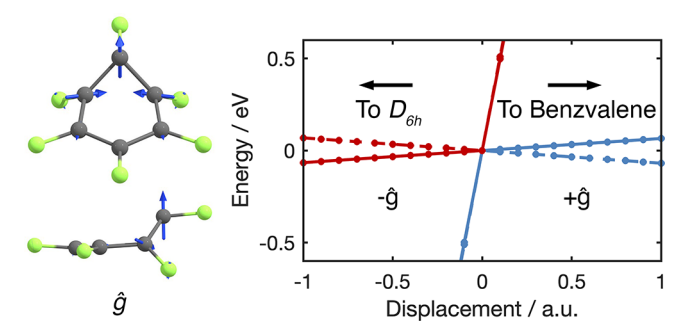


Figure 8. (Left) Minimum Energy CI geometry in HFB with atomwise contributions to the $\hat{\mathbf{g}}$ vector. (Right) Cut of the ground (blue) and first excited (red) states along the branching space $\hat{\mathbf{g}}$ vector for HFB (solid) and benzene (dashed).

contributions to the $\hat{\mathbf{g}}$ vector. The ground state reaction pathway that leads away from the MECP toward $-\hat{\mathbf{g}}$ leads to a reformation of the D_{6h} minimum benzene geometry, while $+\hat{\mathbf{g}}$ leads to the formation of benzvalene.

In benzene's branching space, shown by the dashed lines in Figure 8, the excited state surface slopes downward toward the MECP from both $+\hat{\mathbf{g}}$ and $-\hat{\mathbf{g}}$ directions, forming an energetic funnel. The ground state surface shows that relaxation away from the MECP along both $+\hat{g}$ and $-\hat{g}$ directions is also downhill, although $-\hat{\mathbf{g}}$ is overwhelmingly preferred. These surfaces suggest that benzene molecules nonadiabatically relaxing through this MECP will primarily reform the reactant benzene, with a small benzvalene yield. This analysis agrees well with the observed benzvalene isomerization quantum yield of 1%. 11 The branching space of HFB is shifted compared to benzene, such that both of the interacting surfaces increase in energy from $-\hat{\mathbf{g}}$ to $+\hat{\mathbf{g}}$. This subtle difference has profound effects on the photochemistry through this branching space. The excited-state surface no longer forms a funnel. Instead, a downhill pathway exists in the excited state along the $-\hat{\mathbf{g}}$. The ground state surface of HFB is sloped away from $+\hat{g}$, which further disfavors the formation of hexafluoro-benzvalene. The shift in the PES slope is a product of the PJT coupling between the ¹B_{2u} and ¹E_{1g} states, which lowers the energy of the ¹B_{2u} minimum, thereby increasing the curvature of the PES. Thus, while benzvalene is an observed photochemical product for benzene, that reaction pathway is destabilized in HFB, effectively shutting down this reaction channel and enforcing the observed chemoselectivity in the (overall inefficient) photoisomerization.

Simulated Photochemical Dynamics. Static calculations of the PES provide important mechanistic insight but lack

information on the dynamic molecular evolution or the relative rates of competing excited-state processes. To understand the time-resolved excited state structural dynamics of HFB, an ensemble of gas-phase nonadiabatic dynamics trajectories are computed using the surface-hopping including arbitrary coupling method as implemented in the SHARC suite of programs. $^{\rm 33-35}$ Initial conditions for these trajectories were sampled from the Wigner distribution and initialized in the $\rm S_1$ and $\rm S_2$ electronic states. For the trajectories initialized on the $\rm S_2$ state, the $^{\rm 1}E_{\rm 1g}$ degeneracy is broken by the Wigner sampling of nonplanar geometries and the initial state is taken as the lower of the previously degenerate pair. Each trajectory was propagated for 1 ps with a 0.5 fs time step. We propagated 100 trajectories from the $\rm S_1$ state and 400 trajectories from the $\rm S_2$ state.

For the S_1 trajectories, only three reach the ground state in the simulation time, making a statistical analysis of the rate constant unreliable. However, all three of these trajectories reform the HFB reactant upon reaching the ground state. These observations are again in line with the experimentally observed long-lived excited state and low reaction quantum yield.

Although we have not carried out the corresponding experiment, considering the behavior of HFB molecules excited to the S_2 ($^1E_{1g}$) is informative. The time evolution of the state populations for the ensemble of S_2 trajectories is shown in the top panel in Figure 9. 397 (99.25%) of these trajectories nonadiabatically relaxed to the S_1 state, and 189

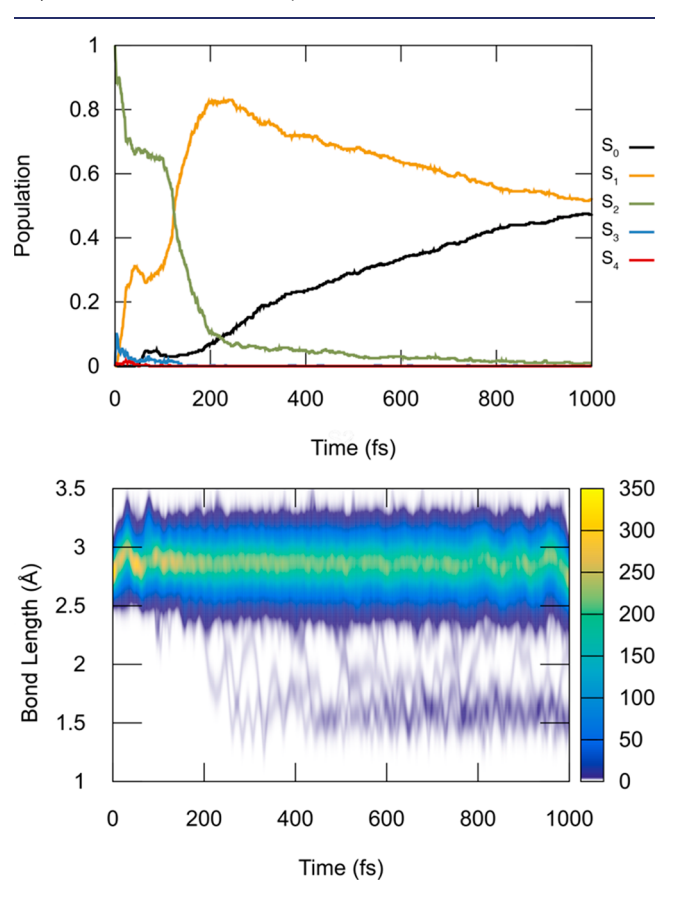


Figure 9. (Top) Time evolution of the population of each electronic state. Green trace shows S_2 , orange trace shows S_1 , and black trace shows S_0 . (Bottom) Time evolution of reactive C–C bond distance for full ensemble of 400 trajectories.

(47.25%) went on to reach the ground state within the 1 ps simulation window. This is due to the additional kinetic energy provided by initial excitation to a higher-energy electronic state. Kinetic fitting of these populations yields two time constants. The S_2-S_1 relaxation process occurs with a time constant of 129 ± 5 fs, and the S_1-S_0 relaxation fits to a time constant of 1180 ± 90 fs. The initial S_2-S_1 relaxation agrees well with the previously determined values 0.10-0.54 ps based on femtosecond time-resolved ion yield measurements for gasphase HFB.

Trajectories deposited on the S_1 surface at the S_2/S_1 conical intersection are deposited near the S_1 minimum but with more kinetic energy than those prepared in the FC region and consequently relax faster than the 2.29 ns time constant observed in TCSPC following excitation to S_1 . This result is consistent with the decreasing S_1 fluorescence quantum yield observed in Figure S8.

The bottom of Figure 9 shows the geometric evolution of the 400 trajectories initialized on S_2 throughout the simulation time. Of the 189 trajectories which reach the ground state surface in the simulation time, 96.8% (183) of these follow a reaction channel that reverts to the HFB reactant, similar to the S_1 -initialized trajectories. However, the remaining 6 trajectories follow a different reaction channel, which does not reform HFB and instead forms the experimentally observed photoproduct, Dewar-HFB. These trajectories appear in the figure at a reactive bond length of <2 Å. While statistical analysis of such a small number of trajectories is unreliable, these data do show that the isomerization reaction can occur directly from nonadiabatic relaxation to the ground state through higher-energy geometries in the S_1/S_0 crossing seam.

Further, none of the photochemically productive trajectories pass through a ground state biradical intermediate, as was proposed by Varma et al. Instead, the softening of the $^{1}B_{2u}$ surface along the e_{2u} vibrational modes promotes molecular vibrations that resemble the Dewar-HFB photoproduct while simultaneously rendering the competing photochemical pathway unfavorable. This is sufficient to produce a small yield of Dewar-HFB from an ensemble of photoexcited HFB molecules, on the order of 1%.

It would appear from our analysis that under the conditions typically used in synthesis (254 nm, 80 W, 8 h), the rather small fraction of molecules born on S_2 may be responsible for the scant photoproduct formed. Why this photochemical preparation works at all under synthesis conditions would seem to come down to the product accumulating slowly over long irradiation times due to the kinetic stability of Dewar-HFB and its lack of absorption in the near-UV region.

It is thus clear that the strength of hexafluorobenzene derivatives as synthetic reagents, in contrast to hydrogenated analogs, is not just the presence of a pathway toward Dewar-HFB on S_1 but a *strict* chemoselective photoproduct formation. In the demonstration of this reaction by Burns et al., the ratio of photons to molecular reagents was 168:1 and achieved a 41% synthetic yield. Interpreting this through the lens of these results shows that although most absorption events result in the reformation of the D_{6h} HFB, provided there is a small but exclusive pathway leading to Dewar-HFB, constant upcycling of the HFB by using a high molar excess of photons still yields an effective reaction.

CONCLUSIONS

HFB and its derivatives are photochemically reactive moieties employed synthetically for their photochemical chemoselective isomerization to Dewar-HFB and its analogs. Ultrafast transient absorption spectroscopy, multireference calculations, and nonadiabatic molecular dynamics simulations have been employed to understand the chemoselectivity, which makes this highly inefficient reaction still synthetically useful. Experimental and simulated absorption spectra show that the perfluoro effect is responsible for lowering the energy of the ${}^{1}\mathrm{E}_{1\mathrm{g}}\left(\pi\sigma^{*}\right)$ state to S_{2} , 0.42 eV above the ${}^{1}\mathrm{B}_{2\mathrm{u}}\left(\pi\pi^{*}\right)$ state. As a result, these states are then vibronically coupled along e211 vibrational modes, distorting the excited state minimum geometry toward the Dewar-HFB product. This perturbation of the potential energy surface creates a barrier toward hexafluoro-benzvalene, which enforces the Dewar-HFB chemoselectivity despite it still being a disfavored channel when compared with reformation of the D_{6h} reactant. These results demonstrate that the internal 4π electrocyclic ring closing is promoted by the electronegative perfluoro effect. Molecular dynamics simulations of photoexcitation to higher electronic states suggest that this would further increase the reaction rate toward Dewar-HFB formation, but this would require experimental confirmation to determine the magnitude of yield enhancement. This work serves as a foundation for understanding the photochemistry of highly fluorinated systems, paving the way for the targeted synthesis of highvalue strained materials.

EXPERIMENTAL SECTION

Computational Methods. The complete active space self-consistent field (CAS) method, as implemented in OpenMolcas, 36,37 has been used to model the photochemical isomerization of hexafluorobenzene with a 6 electron, 7 orbital active space shown in Figure 10. The lowest-energy C–F σ^* orbital is in the active space

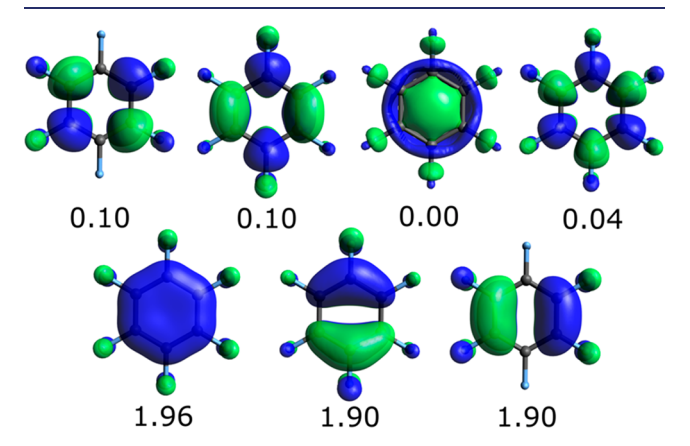


Figure 10. Orbitals included in the CASSCF active space and their average occupation in the ground state wavefunction. Orbitals are computed at the SA-10-CAS(6,7)/aug-cc-pVDZ level.

as previous experimental and computational studies on hexafluor-obenzene show that this orbital is energetically stabilized to a level at or below the lowest π^* orbital due to the perfluoro effect. This σ^* orbital can participate in some of the lowest-lying excited states, and therefore must be included in the active space for an accurate description of, at least, the vertical excitation region of the PES. To account for dynamic electron correlation, CAS energies were corrected with second-order perturbation theory, including electronic

state interactions with extended multistate formulation (XMS-CASPT2).³⁸

Absorption and Emission Spectra. The vibrationally resolved absorption and emission spectra were simulated by first optimizing the ground and excited state minimum energy geometries and computing their respective vibrational frequencies. The overlap between these ground and excited state vibrational wavefunctions (Franck—Condon factors) were then calculated using the harmonic approximation, as implemented in ezSpectrum. ²⁶ Though the excited state minimum geometry has a small dipole moment of 0.2 D, no solvent model was included for consistency with the ground state calculation.

The intensities of vibrational bands were computed for combination bands of 13 vibrational normal modes with 30 vibrational quanta distributed among them. The 13 bands were selected by running a vibronic spectrum analysis on all possible vibrational degrees of freedom but with a limit of 9 quanta per band. Any degree of freedom which contributed to less than 1% of the peaks in that spectrum were eliminated. The geometries, normal modes, and vibrational frequencies were taken from the optimized minimum geometries on the corresponding PES at the CAS(6,7)/aug-cc-PVDZ level.

The classically sampled electronic absorption spectrum was simulated from 164 geometries taken from a single ground-state *ab initio* molecular dynamics trajectory (300 K). The trajectory was first equilibrated for 50 fs at 300 K, followed by a 450 fs production simulation. The snapshots used in the absorption spectrum were randomly sampled from this trajectory, and the absorption energies and oscillator strengths were computed at the XMS-CASPT2(6,7)/aug-cc-PVDZ level. For each state, the average oscillator strength was computed and the individual oscillator strengths were then binned in energy space and the resultant distributions were fitted to a single area normalized Gaussian distribution. The fitted Gaussians were then normalized to the averaged oscillator strengths and converted to molar absorptivities according to Calculation S2. This was then rebinned in wavelength space. No further broadening was used. The histograms and fitted Gaussian functions are shown in Figure S10.

Non-Adiabatic Molecular Dynamics. Photochemical reaction dynamics were simulated using the "surface hopping including arbitrary couplings" algorithm implemented in the SHARC suite of programs. The standard SHARC surface hopping scheme was employed for all simulations. Initial conditions for each trajectory were sampled from the Wigner distribution in the ground state. An ensemble of 100 trajectories was initialized in the S₁ and S₂ electronic states; an additional 300 trajectories were initialized in the S2 state. Trajectories were propagated for 1 ps with the NVE ensemble and a time step of 0.5 fs with an energy based decoherence correction.³⁵ The decoherence parameter was set to 0.1 hartree. The electronic structure at each time step was computed for the five lowest energy singlet states at the SA-5-CAS(6,6)'/ANO-S-VDZP level. The (6,6)active space used here eliminates the highest-energy π^* orbital from the (6,7) space described above. This was previously reported to improve the ordering of electronic states in conjugated systems when a CASPT2 correction is not performed.³¹ CASSCF(6,7) predicts that the S_2 state has doubly excited $(\pi^*\pi^*)$ character, which is corrected via XMS-CASPT2 to the level of S7. This intruder state is absent from the frontier excited states in CASSCF(6,6)'. The dynamics simulations employ the ANO-S-VDZP basis set; it achieves comparable accuracy to the aug-cc-pVDZ basis at a computational cost comparable to cc-pVDZ.40

The kinetics were fit to a three state sequential model of the following form:

$$P_{S1}(t) = \frac{\tau_{10} P_{S2}(0)}{\tau_{10} - \tau_{21}} (e^{-t/\tau_{10}} - e^{-t/\tau_{21}})$$

where P_{S2} and P_{S1} are the population of the S_2 and S_1 states, respectively. τ_{21} is the time constant of transfer between S_2 and S_1 and τ_{10} is the time constant of population transfer between S_1 and S_0 . The values of τ_{21} and τ_{10} are determined to be (129.4 \pm 4.6) fs and

 (1180.7 ± 89.4) fs. The statistical errors are estimated by a 100 cycle bootstrapping procedure.

Sample Preparation and Purification. Hexafluorobenzene (Sigma-Aldrich, >99% purity) was used without further purification for the transient absorption and TCSPC measurements. For fluorescence and UV—vis experiments, HFB was purified by fractional distillation at 120 °C to remove fluorescent impurities. All HFB solutions were made with ethanol (VWR, 200 proof).

Distillation was performed using a fractional distillation column and a water jacketed condenser. The HFB was boiled in a round-bottom flask using mineral oil to a bath temperature of $120\,^{\circ}$ C. The first few drops of the distillate, the head, was removed from the collection flask and discarded. The first distillate was then collected and redistilled again. The HFB used in long-wavelength UV—vis experiments, both distilled and nondistilled, was then diluted via serial dilution and used for the experiment.

Tryptophan (Sigma-Aldrich, 97%) was used as the fluorescence quantum yield standard without further purification.

Absorption and Fluorescence Measurements. All absorption measurements were performed on a Cary 60 UV—vis spectrometer with ethanol in a quartz 1 cm cuvette used to set the baseline. The fluorescence measurements were carried out on a Horiba Jobin Yvon FluoroMax-3 fluorometer. A Starna Cells spectrosil 1 cm path length cuvette was used for all measurements.

The emission and excitation spectra were obtained during the same experiment. The excitation was fixed at a given wavelength as the emission spectrum was scanned between 230 and 500 nm. The excitation was stepped in 2 nm increments between 200 and 300 nm and again the emission spectrum was collected. The integration time was 100 ms with bandwidths for the excitation and emission set at 5 nm. To create the excitation spectrum for Figure S8, the entire 2D array was integrated along the emission axis to collapse it down to a 1D array with excitation wavelength as the only variable.

In the quantum yield measurements, the absorbances of the HFB and tryptophan/buffer solutions were 0.034 OD and 0.049 OD, respectively, at the excitation wavelength of 270 nm. The buffer solution, used as the solvent for tryptophan, produced no fluorescence at 270 nm excitation. For the QY fluorescence measurements, the bandwidths of both the excitation and emission monochromators were set to 2 nm and scanned in 0.25 nm increments with each point integrated for 100 ms. The fluorescence from the pure ethanol was subtracted off the HFB intensity.

The wavelength-dependent fluorescence quantum yield (Figure S8) was calculated by normalizing the HFB absorption and integrated excitation to 1 at 270 nm. The QY was calculated by dividing the integrated excitation spectrum by the absorption spectrum and scaling by 0.029—the fluorescence quantum yield of tryptophan at 270 nm.

Temperature-Dependent Fluorescence. Temperature-dependent fluorescence was recorded using a QuantaMaster Xe arc lamp spectrofluorometer equipped with an R1527 PMT detector loaded with a 71 μ M solution of HFB in ethanol in a 1 cm screw-top quartz Starna Cells cell. The excitation monochromator was centered at 255 nm, while the emission monochromator was stepped in 1 nm intervals from 300 to 500 nm. The integration time was set to 1 s, and the excitation and emission monochromator bandwidth slits were set to 5 nm. Scans were averaged twice. The sample cell is immersed in a temperature-controlled flowing water bath which, was varied between 23 and 56 °C.

Femtosecond Transient Absorption. The 35 fs, 800 nm output of a Coherent Legend amplifier was taken to generate both the pump and probe beams. 10% was sent to generate the white light continuum probe. The time delay between the pump and probe was generated by sending the probe down a translating gold-plated cube corner retroreflector. The white light was generated by focusing the fundamental onto a 2 mm rotating CaF $_2$ disk. The supercontinuum was collimated and then focused on the sample by two off-axis parabolic mirrors. The transmitted probe beam was collimated and then focused onto a 120 μm slit of a grating Czerny-Turner monochromator. The light was then dispersed across a 256-pixel array to achieve a detected continuum spanning from 345 to 650 nm.

The deep UV (DUV) pump beam was generated in a home-built noncolinear optical parametric amplifier (NOPA) pumped with 60 mW of 800 nm (35 fs). About 10% of the fundamental was focused on a sapphire disk to generate a white light seed. The remaining fundamental was directed and focused on an SHG BBO to generate the 400 nm pump. The signal was generated by combining the weak white light seed onto a thin BBO crystal with the 400 nm pump. The signal generated, 510 nm, is then passed through a prism compressor to compensate for spectral chirp of the visible beam and increase DUV SHG efficiency. The signal is then sent through another BBO crystal to generate the second harmonic of 510 nm, 255 nm. The DUV beam was sent through two calcium fluoride prisms to compress the UV pulses. The DUV pulse was focused to a spot size of 360 μm with a pulse energy of 580 nJ, 5 cm, in front of the gravity jet sample. A gravity jet was used in place of a sample flow cell to reduce nonlinear effects such as cross-phase modulation and possible signal from the glass and reduce temporal walk off of the pump and probe pulses due to spectral chirp, optimizing the time resolution. For this setup, the sample was contained within an upper reservoir that flowed downward, forming a thin sheet across a loop of 0.005 in. tungsten wire, forming a jet with a thickness of 130 μ m at the pumpprobe overlap. The pump and probe were overlapped at the gravity jet sheet in the center of the loop to minimize lensing effects. The reservoir height was maintained at a constant height of ~40 cm to ensure a consistent sheet thickness throughout the experiment.

To compensate for the low signal-to-noise ratio, the spectra were averaged in delay time using a 10 point moving mean algorithm. This improves the signal-to-noise ratio from 16 to 87 when assessed at the same 300 fs, 550 nm point.

Time-Correlated Single Photon Counting. The fluorescence lifetime of HFB was measured using Time-Correlated Single Photon Counting (TCSPC). 532 nm, produced as the second harmonic of an Alphalas PULSELAS-A-266-300-SP Nd:YAG laser operating at 10 kHz, was focused into a fourth harmonic generation (FHG) crystal to yield 266 nm, which was used to pump the sample. The sync trigger is provided by the residual 532 nm passing through the 266 nm pick off the high reflector. This residue was used to trigger a Becker & Hickl GmbH PHD-400-N fast photodiode sync. The bandwidth of the laser is 1.9 at 266 nm.

The experiment was done in a 1 cm quartz cuvette with a sample absorption of 0.043 OD at 266 nm. The total time acquisition of the TCSPC measurements was 60 min with an intensity of 150 mW/cm². The power was set such that the number of detected photons was lower than $\sim \!\! 1\%$ of the laser repetition rate. This was to reduce the probability of two detected events per laser shot, which can distort the timed-binned histogram.

The monochromator used was a CVI Digikrom CM-112 1/8 Monochromator. The monochromator was set at 370 nm, the height of the HFB emission spectrum. The slit widths were set at 16 nm by using static metal slits. A large bandwidth was required due to low signal level.

ASSOCIATED CONTENT

Supporting Information

The Supporting Information is available free of charge at https://pubs.acs.org/doi/10.1021/jacs.1c01506.

Vibrational normal modes, excited state minimum energy path, additional transient absorption spectra, fluorescence spectra, TA time delays, TA temporal fitting, fluorescence lifetime fitting, simulated absorption histograms, and calculation formulas (PDF)

AUTHOR INFORMATION

Corresponding Authors

Stephen E. Bradforth – Department of Chemistry, University of Southern California, Los Angeles, California 90089-0482, United States; o orcid.org/0000-0002-6164-3347; Email: stephen.bradforth@usc.edu

Steven A. Lopez — Department of Chemistry and Chemical Biology, Northeastern University, Boston, Massachusetts 02115, United States; orcid.org/0000-0002-8418-3638; Email: s.lopez@northeastern.edu

Authors

Jordan M. Cox – Department of Chemistry and Chemical Biology, Northeastern University, Boston, Massachusetts 02115, United States

Matthew Bain – Department of Chemistry, University of Southern California, Los Angeles, California 90089-0482, United States

Michael Kellogg – Department of Chemistry, University of Southern California, Los Angeles, California 90089-0482, United States; orcid.org/0000-0002-3476-2455

Complete contact information is available at: https://pubs.acs.org/10.1021/jacs.1c01506

Author Contributions

§These authors contributed equally to the manuscript.

Notes

The authors declare no competing financial interest.

ACKNOWLEDGMENTS

J.C. and S.A.L. acknowledge Dr. Jingbai Li for helpful discussion on the NAMD trajectories. S.A.L. and S.B. acknowledge the Office of Naval Research (ONR N00014-18-1-2659) for funding this research. S.A.L. also acknowledges the National Science Foundation (NSF-OAC-1940307) for funding. J.C. and S.A.L. appreciate the assistance from the Northeastern Research Computing Team and access to the computing resources of the Discovery cluster. M.K., M.B., and S.E.B. acknowledge the resources at the USC Agilent Center of Excellence in Biomolecular Characterization.

REFERENCES

- (1) Watson, W. H.; McMordie, W. C.; Lands, L. G. Polymerization of Alkynes by Ziegler-type Catalyst. *J. Polym. Sci.* **1961**, *55* (161), 137–144.
- (2) Shirakawa, H.; Louis, E. J.; MacDiarmid, A. G.; Chiang, C. K.; Heeger, A. J. Synthesis of Electrically Conducting Organic Polymers: Halogen Derivatives of Polyacetylene, (CH) x. J. Chem. Soc., Chem. Commun. 1977, 0 (16), 578–580.
- (3) Gould, G. L.; Eswara, V.; Trifu, R. M.; Castner, D. G. Polydifluoroacetylene, Polychlorofluoroacetylene, and Polydichloroacetylene. *J. Am. Chem. Soc.* **1999**, *121* (15), 3781–3782.
- (4) Boswell, B. R.; Mansson, C. M. F.; Cox, J. M.; Jin, Z.; Romaniuk, J. A. H.; Lindquist, K. P.; Cegelski, L.; Xia, Y.; Lopez, S. A.; Burns, N. Z. Mechanochemical Synthesis of an Elusive Fluorinated Polyacetylene. *Nat. Chem.* **2021**, *13* (1), 41–46.
- (5) Ward, H. R.; Wishnok, J. S. Vacuum Ultraviolet Photolysis of Liquid Benzene. Photoisomerization of Benzene to Dewar Benzene. *J. Am. Chem. Soc.* **1968**, 90 (4), 1085–1086.
- (6) Bryce-Smith, D.; Gilbert, A.; Orger, B. H. Photoaddition of Cis-Cyclo-Octene to Hexafluorobenzene. *J. Chem. Soc. D* **1969**, 0 (14), 800b–8802.
- (7) Zupan, M.; Šket, B. Photochemistry of Fluorosubstituted Aromatic and Heteroaromatic Molecules. *Isr. J. Chem.* **1978**, *17* (1–2), 92–99.
- (8) Šket, B.; Zupančič, N.; Zupan, M. Photochemistry of Organo-Halogenic Molecules. Part 20. The Effect of Cycloalkene Structure on the [2 + 2] Photocycloaddition to Hexafluorobenzene. *J. Chem. Soc., Perkin Trans.* 1 1987, 0 (0), 981–985.

- (9) Lemal, D. M. Hexafluorobenzene Photochemistry: Wellspring of Fluorocarbon Structures. *Acc. Chem. Res.* **2001**, 34 (8), 662–671.
- (10) Haller, I. Photoisomerization of Hexafluorobenzene. *J. Am. Chem. Soc.* **1966**, 88 (9), 2070–2071.
- (11) Wilzbach, K. E.; Ritscher, J. S.; Kaplan, L. Benzvalene, the Tricyclic Valence Isomer of Benzene. *J. Am. Chem. Soc.* **1967**, 89 (4), 1031–1032.
- (12) Blair, J. M.; Bryce-Smith, D. The Photoisomerization of Benzene to Fulvene. *Proc. Chem. Soc.* **1957**, *0*, 287–288.
- (13) Zgierski, M. Z.; Fujiwara, T.; Lim, E. C. Photophysics of Aromatic Molecules with Low-Lying $\pi\sigma^*$ States: Fluorinated Benzenes. *J. Chem. Phys.* **2005**, *122* (14), 144312.
- (14) Clark, I. D.; Frost, D. C. A Study of the Energy Levels in Benzene and Some Fluorobenzenes by Photoelectron Spectroscopy. *J. Am. Chem. Soc.* **1967**, 89 (2), 244–247.
- (15) Camaggi, G.; Gozzo, F.; Cevidalli, G. Para -Bonded Isomers of Fluoroaromatic Compounds. *Chem. Commun.* **1966**, 0 (10), 313–314.
- (16) Haller, I. Kinetics and Mechanism of the Photochemical Valence Tautomerization of Hexafluorobenzene. *J. Chem. Phys.* **1967**, 47 (3), 1117–1125.
- (17) Suijker, J. L.; Huizer, A. H.; Varma, C. A. G. O. Picosecond Spectroscopy in Study of the Photoinduced Isomerization of Hexafluorobenzene. *Laser Chem.* **1986**, *6* (5), 333–347.
- (18) Cordes, T.; Herzog, T. T.; Malkmus, S.; Draxler, S.; Brust, T.; DiGirolamo, J. A.; Lees, W. J.; Braun, M. Wavelength and Solvent Independent Photochemistry: The Electrocyclic Ring-Closure of Indolylfulgides. *Photochem. Photobiol. Sci.* **2009**, 8 (4), 528–534.
- (19) Studzinski, H.; Zhang, S.; Wang, Y.; Temps, F. Ultrafast Nonradiative Dynamics in Electronically Excited Hexafluorobenzene by Femtosecond Time-Resolved Mass Spectrometry. *J. Chem. Phys.* **2008**, *128* (16), *164314*.
- (20) Motch, C.; Giuliani, A.; Delwiche, J.; Limão-Vieira, P.; Mason, N. J.; Hoffmann, S. V.; Hubin-Franskin, M.-J. Electronic Structure of Hexafluorobenzene by High-Resolution Vacuum Ultraviolet Photo-Absorption and He(I) Photoelectron Spectroscopy. *Chem. Phys.* **2006**, 328 (1–3), 183–189.
- (21) Holland, D. M. P.; Shaw, D. A.; Stener, M.; Decleva, P. A Study of the Valence Shell Electronic Structure of Hexafluorobenzene Using Photoabsorption and Photoelectron Spectroscopy, and TDDFT Calculations. J. Phys. B: At., Mol. Opt. Phys. 2009, 42 (24), 245201.
- (22) Philis, J.; Bolovinos, A.; Andritsopoulos, G.; Pantos, E.; Tsekeris, P. A Comparison of the Absorption Spectra of the Fluorobenzenes and Benzene in the Region 4.5–9.5 eV. *J. Phys. B: At. Mol. Phys.* **1981**, *14* (19), 3621.
- (23) Mondal, T.; Reddy, S. R.; Mahapatra, S. Photophysics of Fluorinated Benzene. III. Hexafluorobenzene. *J. Chem. Phys.* **2012**, 137 (5), 054311.
- (24) Taniguchi, M.; Lindsey, J. S. Database of Absorption and Fluorescence Spectra of >300 Common Compounds for Use in PhotochemCAD. *Photochem. Photobiol.* **2018**, *94* (2), 290–327.
- (25) Berlman, I. B. Handbook of Fluorescence Spectra of Aromatic Molecules; Academic Press: New York, 1971; p 47.
- (26) Mozhayskiy, V. A.; Krylov, A. I. ezSpectrum; 2021.
- (27) Goodman, L.; Ozkabak, A. G.; Thakur, S. N. A Benchmark Vibrational Potential Surface: Ground-State Benzene. *J. Phys. Chem.* **1991**, 95 (23), 9044–9058.
- (28) Palmer, I. J.; Ragazos, I. N.; Bernardi, F.; Olivucci, M.; Robb, M. A. An MC-SCF Study of the S₁ and S₂ Photochemical Reactions of Benzene. *J. Am. Chem. Soc.* **1993**, *115* (2), 673–682.
- (29) Nakashima, N.; Sumitani, M.; Ohmine, I.; Yoshihara, K. Nanosecond Laser Photolysis of the Benzene Monomer and Eximer. *J. Chem. Phys.* **1980**, 72 (4), 2226–2230.
- (30) Miyazaki, M.; Fujii, M. Real Time Observation of the Excimer Formation Dynamics of a Gas Phase Benzene Dimer by Picosecond Pump-Probe Spectroscopy. *Phys. Chem. Chem. Phys.* **2015**, *17* (39), 25989–25997.

- (31) Thompson, A. L.; Martínez, T. J. Time-Resolved Photoelectron Spectroscopy from First Principles: Excited State Dynamics of Benzene. *Faraday Discuss.* **2011**, *150* (0), 293–311.
- (32) Galvan, I. F.; Delcey, M. G.; Pedersen, T. B.; Aquilante, F.; Lindh, R. Analytical State-Average Complete-Active-Space Self-Consistent Field Nonadiabatic Coupling Vectors: Implementation with Density-Fitted Two-Electron Integrals and Application to Conical Intersections. *J. Chem. Theory Comput.* **2016**, *12* (8), 3636–3653.
- (33) Mai, S.; Richter, M.; Hendl, M.; Menger, M. F. S. J.; Atkins, A.; Ruckenbauer, M.; Plasser, F.; Ibele, L. M.; Kropf, S.; Oppel, M.; Marquetand, P.; González, L. SHARC2.1: Surface Hopping Including Arbitrary Couplings—Program Package for Non-Adiabatic Dynamics; 2021.
- (34) Richter, M.; Marquetand, P.; González-Vázquez, J.; Sola, I.; González, L. SHARC: Ab Initio Molecular Dynamics with Surface Hopping in the Adiabatic Representation Including Arbitrary Couplings. J. Chem. Theory Comput. 2011, 7 (5), 1253–1258.
- (35) Mai, S.; Marquetand, P.; González, L. Nonadiabatic Dynamics: The SHARC Approach. Wiley Interdiscip Rev. Comput. Mol. Sci. 2018, 8 (6), No. e1370.
- (36) Galván, I. F.; Vacher, M.; Alavi, A.; Angeli, C.; Aquilante, F.; Autschbach, J.; Bao, J. J.; Bokarev, S. I.; Bogdanov, N. A.; Carlson, R. K.; Chibotaru, L. F.; Creutzberg, J.; Dattani, N.; Delcey, M. G.; Dong, S. S.; Dreuw, A.; Freitag, L.; Frutos, L. M.; Gagliardi, L.; Gendron, F.; Giussani, A.; González, L.; Grell, G.; Guo, M.; Hoyer, C. E.; Johansson, M.; Keller, S.; Knecht, S.; Kovačević, G.; Källman, E.; Manni, G. L.; Lundberg, M.; Ma, Y.; Mai, S.; Malhado, J. P.; Malmqvist, P. Å.; Marquetand, P.; Mewes, S. A.; Norell, J.; Olivucci, M.; Oppel, M.; Phung, Q. M.; Pierloot, K.; Plasser, F.; Reiher, M.; Sand, A. M.; Schapiro, I.; Sharma, P.; Stein, C. J.; Sørensen, L. K.; Truhlar, D. G.; Ugandi, M.; Ungur, L.; Valentini, A.; Vancoillie, S.; Veryazov, V.; Weser, O.; Wesołowski, T. A.; Widmark, P.-O.; Wouters, S.; Zech, A.; Zobel, J. P.; Lindh, R. OpenMolcas: From Source Code to Insight. J. Chem. Theory Comput. 2019, 15 (11), 5925–5964.
- (37) Aquilante, F.; Autschbach, J.; Baiardi, A.; Battaglia, S.; Borin, V. A.; Chibotaru, L. F.; Conti, I.; De Vico, L.; Delcey, M.; Galván, I. F.; Ferré, N.; Freitag, L.; Garavelli, M.; Gong, X.; Knecht, S.; Larsson, E. D.; Lindh, R.; Lundberg, M.; Malmqvist, P. Å.; Nenov, A.; Norell, J.; Odelius, M.; Olivucci, M.; Pedersen, T. B.; Pedraza-González, L.; Phung, Q. M.; Pierloot, K.; Reiher, M.; Schapiro, I.; Segarra-Martí, J.; Segatta, F.; Seijo, L.; Sen, S.; Sergentu, D.-C.; Stein, C. J.; Ungur, L.; Vacher, M.; Valentini, A.; Veryazov, V. Modern Quantum Chemistry with [Open]Molcas. J. Chem. Phys. 2020, 152 (21), 214117.
- (38) Shiozaki, T.; Györffy, W.; Celani, P.; Werner, H.-J. Communication: Extended Multi-State Complete Active Space Second-Order Perturbation Theory: Energy and Nuclear Gradients. *J. Chem. Phys.* **2011**, *135* (8), 081106.
- (39) Granucci, G.; Persico, M.; Zoccante, A. Including Quantum Decoherence in Surface Hopping. *J. Chem. Phys.* **2010**, *133* (13), 134111.
- (40) Plasser, F.; Mewes, S. A.; Dreuw, A.; González, L. Detailed Wave Function Analysis for Multireference Methods: Implementation in the Molcas Program Package and Applications to Tetracene. *J. Chem. Theory Comput.* **2017**, *13* (11), 5343–5353.
- (41) Tauber, M. J.; Mathies, R. A.; Chen, X.; Bradforth, S. E. Flowing Liquid Sample Jet for Resonance Raman and Ultrafast Optical Spectroscopy. *Rev. Sci. Instrum.* **2003**, 74 (11), 4958–4960.